Dynamics of growing carbon nanotube interfaces probed by machine learning-enabled molecular simulations

Daniel Hedman

daniel.hedman@ltu.se

   Institute for Basic Science   https://orcid.org/0000-0003-1542-6170

Ben McLean

   RMIT University

Christophe Bichara

   CNRS and Aix-Marseille University   https://orcid.org/0000-0002-7226-3155

Shigeo Maruyama

   The University of Tokyo   https://orcid.org/0000-0003-3694-3070

J. Andreas Larsson

   Luleå University of Technology   https://orcid.org/0000-0003-3455-2877

Feng Ding

   Shenzhen Institute of Advanced Technology, Chinese Academy of Sciences

---

Additional Declarations: There is **NO** Competing Interest.

Title: Dynamics of growing carbon nanotube interfaces probed by machine learning-enabled molecular simulations

Authors: Daniel Hedman[1*], Ben McLean[1, 2], Christophe Bichara[3], Shigeo Maruyama[4], J. Andreas Larsson[5] and Feng Ding[1, 6, 7*]

Affiliations:

[1]Center for Multidimensional Carbon Materials (CMCM), Institute for Basic Science (IBS), Ulsan, 44919, Republic of Korea

[2]School of Engineering, RMIT University, Victoria, 3001, Australia

[3]Aix-Marseille Univ, CNRS, CINaM, UMR7325, Marseille, 13288, France

[4]Department of Mechanical Engineering, The University of Tokyo, Tokyo, 113-8656, Japan

[5]Applied Physics, Division of Materials Science, Department of Engineering Sciences and Mathematics, Luleå University of Technology, Luleå, 971 87, Sweden

[6]Department of Materials Science and Engineering, Ulsan National Institute of Science and Technology (UNIST), Ulsan, 44919, Republic of Korea

[7]Faculty of Materials Science and Engineering, Institute of Technology for Carbon Neutrality, Shenzhen Institute of Advanced Technology Chinese Academy of Sciences, Shenzhen, 518055, China

*Corresponding authors: Daniel Hedman: daniel.hedman@ltu.se and Feng Ding: f.ding@siat.ac.cn

Abstract: **Carbon nanotubes (CNTs), hollow cylinders of carbon[1] with diameters in the nanometer range, hold great promise for advanced technologies[2-5], provided their structure is controlled and remains uniform throughout their length[6-9]. Their growth, facilitated by a metal catalyst, takes place at high temperatures across a tube-catalyst interface comprising a few tens of carbon atoms. During growth, the structure, and properties of CNTs are defined but defects can alter them[10]. These defects are believed to form and heal at the tube-catalyst interface although an understanding of these mechanisms at the atomic-level is still lacking[11, 12]. Here, using molecular dynamics simulations driven by a machine learning force field[13] (MLFF) we developed, DeepCNT-22, we unveil the mechanisms of CNT formation from nucleation to growth including defect formation and healing. We find the tube-catalyst interface to be highly dynamic during growth, with large fluctuations in the chiral structure of the CNT-edge. This contradicts the previous notion of a continuous spiral growth mode[14], but confirms that the growing tube edge exhibits significant configurational entropy[15]. We demonstrate that defects form stochastically at the tube-catalyst interface, however, under low growth rates and high temperatures, healing becomes more efficient than formation, allowing CNTs to grow defect-free to seemingly unlimited lengths. These insights, not readily available via experiments, demonstrate the remarkable power of MLFF-driven simulations and fill long-standing gaps in our understanding of CNT growth mechanisms.**

Main Text:

Carbon nanotubes (CNTs) stand as an iconic example of low-dimensional materials. These hollow tubes, composed of carbon atoms arranged in a hexagonal lattice[1], have diameters of only a few nanometers yet can extend several centimeters in length[7-9]. Over the past three decades, researchers have discovered remarkable mechanical[16], thermal[17], electrical[18], and optical[19] properties of CNTs. Their electrical properties can be precisely tailored by adjusting the orientation of the hexagonal lattice relative to the tube axis[6], represented by two chiral indices (n, m), making CNTs highly attractive for advanced technologies[2-5]. However, maintaining uniform properties over their entire length is challenging, as the chirality must be constant along the length of the tube. Changes in chirality result from defects in the tube wall, typically in the form of pentagons or heptagons which form during synthesis[10]. A typical centimeter-long single-walled carbon nanotube (SWCNT) consists of approximately 10^{10} hexagons, thus the defect concentration must be less than 0.1 parts per million to produce long defect-free SWCNTs.

Catalytic chemical vapor deposition (CCVD) has emerged as the most prominent method for synthesizing CNTs, employing metal nanoparticles as catalysts to decompose hydrocarbon gas at high temperatures[11]. From these decomposed hydrocarbons, an initial CNT-cap nucleates on the catalyst. If the thermodynamic driving force is large enough, the cap will lift off the catalyst and form the tip of the developing CNT[20]. Which elongates (grows) through continuous incorporation of carbon atoms at the interface between the CNT-edge and the catalyst (the tube-catalyst interface). For SWCNTs, the rate of carbon incorporation (growth rate) spans from 0.5 to 10 carbon atoms per microsecond[7, 8, 11, 21, 22]. Fundamental understanding of the mechanisms behind CNT nucleation and growth *i.e.* the evolution of the tube-catalyst interface is crucial for producing long defect-free CNTs with uniform properties throughout their length. While experimental studies, particularly *in situ* transmission electron microscopy, have provided valuable insights[23-25], a

comprehensive atomic-level understanding of CNT growth has not yet been achieved through experimental measurements alone. Instead, computational studies, especially molecular dynamics (MD), have played a crucial role in revealing aspects of the growth mechanisms[12]. However, MD simulations have been methodologically limited in accurately exploring the timescales necessary for defect-free growth without the use of additional biasing methods[26, 27]. Consequently, the growth of defect-free CNTs by unbiased MD simulations remains elusive[28], and many questions related to growth remain unanswered. Namely, the timescale of the nucleation process, how defects form and heal, and the evolution of the tube-catalyst interface during growth—all of which are crucial to understand for controlled growth of long defect-free CNTs.

Leveraging machine learning force fields

An emerging and powerful method for modeling materials at experimentally relevant length and timescales is machine learning force fields[13] (MLFFs). This method involves training machine learning models on a large dataset of atomic configurations (structures) labeled with energies, forces and virials calculated using first principles methods such as density functional theory (DFT). Once trained, MLFFs can predict physical quantities and drive atomistic simulations with the computational efficiency of empirical force fields, all while maintaining the accuracy of DFT or even beyond-DFT methods[29].

In this study, DeepCNT-22, a MLFF based on DeepMD[30] is presented, capable of driving MD simulations of SWCNT growth on iron catalysts. Iron was selected as it is among the most used catalysts in experiments and resides in the middle of the Goldilocks' zone of metals considered as effective catalysts for growth[31, 32].
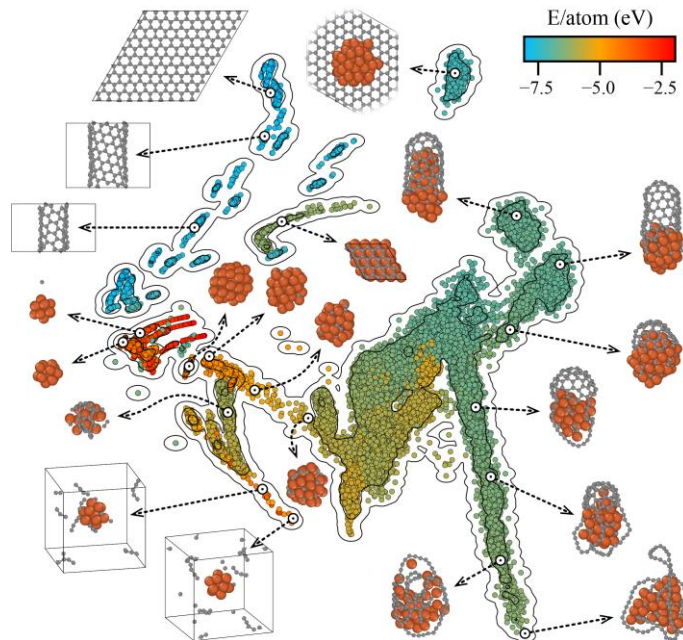
Fig. 1: Sketch-map visualization of the DeepCNT-22 dataset. The sketch-map consists of 22,975 structures where each colored dot represents an individual structure with the color indicating its corresponding energy. Examples of atomic configurations from different regions of the sketch map are shown to provide insight into the diversity of the data set. The orange and grey spheres represent Fe and C atoms, respectively.

DeepCNT-22 enables investigation of the entire SWCNT growth process on near-microsecond timescales, without sacrificing computational accuracy and without employing steering or other biases. A significant challenge in developing MLFFs is creating high-quality, diverse datasets for training. The DeepCNT-22 dataset, shown in Fig. 1 as a sketch-map representation[33], includes a wide variety of structures relevant to SWCNT growth. Each point in the sketch-map denotes a unique structure, with its position determined by principal component analysis on the learned descriptors of the local atomic environments (embeddings).
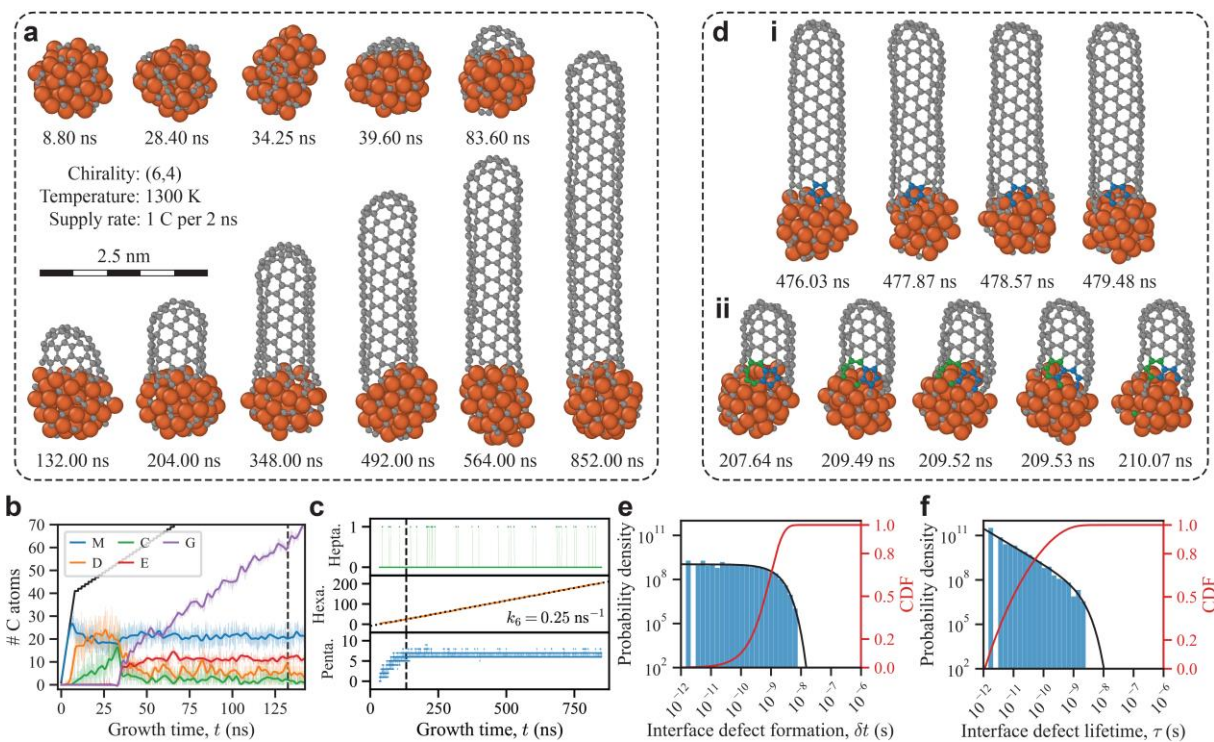
Fig. 2: Growth of a defect-free (6,5) SWCNT on a Fe₅₅ catalyst at a temperature of $T = 1300$ K and a growth rate of $k = 0.5$ ns⁻¹. Panel **a** displays 11 snapshots of the structure during the growth process, and panel **d** illustrates the healing of interface defects **i** 5-ring and **ii** 5-7 pair. The orange and grey spheres represent Fe and C atoms, respectively, in panel **d** blue and green spheres are used to depict C atoms initially belonging to a pentagon and heptagon interface defect, respectively. **b** shows the number of carbon atoms comprising each species, including monomers (M), dimers (D), chains (C), part of the edges (E), and graphitic structures (G), during the early phases of growth. The solid black line is the total number of carbon atoms added to the system, the transparent colored lines represent raw data, and the solid lines is the result of applying a low-pass filter. **C** presents the number of penta-, hexa-, and heptagons during growth, with a linear regression (dotted line) determining the hexagon formation rate, k_6. The dashed vertical line in **b** and **c** marks the time at which the SWCNT-cap is fully formed, $t = 132.41$ ns. **e** and **f** show the probability density function (solid black line) and the cumulative distribution function (CDF) (solid red line) for the time between formation of interface defects, δt, and the interface defect lifetime, τ, during the growth process after the cap is fully formed.

As the atomic configurations illustrate, different regions of the sketch-map correspond to different structures, with clear grouping of similar structures and separation of dissimilar ones. This

highlights the diversity of the dataset and the quality of the learned descriptors. Details on the creation of this dataset as well as training of the DeepCNT-22 MLFF are provided in the Methods section. Verification of the accuracy of DeepCNT-22—including its ability to accurately reproduce the expected broad chirality distribution typically found for iron catalysts and the ratio of SWCNT diameter to catalyst diameter—is provided in Supplementary Information Section 1.

After training, DeepCNT-22 was used to drive MD simulations of SWCNT growth starting from clean iron catalysts. In these simulations, the carbon supply rate, k, and the growth temperature, T, are parameters that influence the growth process. A carbon supply rate of $k \leq 1.0$ ns^{-1} matched with a growth temperature of $1200 \leq T \leq 1500$ K is found to be suitable for growth, as seen in Extended Data Fig. 1. Under these conditions, the growth rate is limited by the carbon supply rate, resulting in a 1:1 correlation between them, thus both terms are used interchangeably. Fig. 2 shows the result of a 4.76 nm long $(n, m) = (6,5)$ SWCNT grown on a Fe$_{55}$ catalyst over 0.852 μs at $T = 1300$ K and $k = 0.5$ ns^{-1}. This corresponds to a growth rate of 5590 μm/s, which is approximately 50 to 1000 times higher than experimentally reported growth rates[7, 8, 11, 21, 22] and lower by a factor of up to 100 compared to previous MD simulations[27, 28, 34-36]. Despite the high growth rate, the resulting SWCNT shown in Fig. 2a is free of defects, demonstrating that defect-free growth can be achieved even at very high growth rates. Additional defect-free SWCNTs grown using DeepCNT-22 can be found in Extended Data Fig. 2. It should be noted that the chirality of these tubes is not predetermined but emerges naturally during the growth simulation. From Fig. 2b, it is evident that growth can be divided into five distinct phases: 1st abundance of carbon monomers inside the catalyst and dimers on the surface, 2nd conversion of monomers and dimers into carbon chains, 3rd rapid conversion of chains into graphitic carbon (pentagons and hexagons), 4th formation of the SWCNT-cap and cap liftoff, and 5th continuous elongation of the tube. Though these five phases have in part been investigated in previous studies[26, 27, 34, 37, 38], here

7

118   the entire process is presented in full and unveils the timescale of each phase. A detailed

119   breakdown of which can be found in Supporting Information Section 2. These five phases,

120   combined with the snapshots in Fig. 2a and Extended Data Video 1, offer comprehensive atomic-

121   level details of SWCNT nucleation and growth.

Defect formation and healing

123   As seen from the snapshot at $t = 852.00$ ns in Fig. 2a, the grown SWCNT is straight and of single

124   chirality, which is only possible if the tube wall consists solely of hexagons. However, this does

125   not mean that only hexagons are formed during growth. Analysis of the number of penta-, hexa-,

126   and heptagons during the 5th phase of growth, to the right of the dashed line in Fig. 2c, reveals a

127   continuous increase in the number of hexagons where the rate of hexagon formation k_6 is half the

128   growth rate, i.e., $k_6 = k/2 = 0.25$ ns[-1]. Moreover, the number of pentagons frequently surpasses

129   the six pentagons that are part of the SWCNT-cap, and heptagons occasionally form.

130   From analysis of the structure during growth (see Extended Data Video 1, 2, and 3), it was found

131   that, like hexagons, penta- and heptagons form at the tube-catalyst interface. Thus, a distinction is

132   made between interface defects (penta- and heptagons near the tube-catalyst interface) and trapped

133   defects (penta- and heptagons incorporated in the tube wall). Having successfully grown defect-

134   free SWCNTs (see Fig. 2a and Extended Data Fig. 2) and verified the presence of both penta- and

135   heptagons during the 5th phase of growth (see Fig. 2c), it is concluded that interface defects are

136   effectively healed during the growth process. Fig. 2di shows an example of healing a pentagon

137   interface defect, while Fig. 2dii exemplifies the healing of a more complex pentagon-heptagon

138   pair. From these and Extended Data Video 2 and 3, key processes involved in the healing of

139   interface defects are identified: etching of the SWCNT-edge, which exposes interface defects to

the metal catalyst, and carbon-carbon bond cleavage facilitated by metal atoms, which hold the broken bond open until a metal atom is replaced by a carbon atom, thus completing the hexagon.

The efficiency of DeepCNT-22 enables growth simulations on experimentally relevant time scales, allowing a statistical analysis of defect formation and lifetimes. During growth of the (6,5) SWCNT shown in Fig. 2, a total of 778 different pentagons were identified, compared to only 26 heptagons. For the pentagons, the time between formation of interface defects, δt, is plotted in Fig. 2e as a log-log histogram. Here it is clear that δt can be modeled using a typical exponential distribution, whose probability density function (PDF) is given by

$$f_{\delta t} = \lambda_1 e^{-\lambda_1 \delta t}. \tag{1}$$

Since the exponential distribution describes the time between events in a Poisson point process, the formation of interface defects can be considered a purely stochastic process. Fitting the cumulative distribution function (CDF) of Eq. (1) to the normalized cumulative sum of the measured values of δt yields $\lambda_1 = 1.08 \cdot 10^9$ s^{-1}. This gives an expected value for the time between formation of interface defects, $\langle \delta t \rangle = 1/\lambda_1 = 0.925$ ns. From the CDF, it is also evident that there is a 99% probability that interface defects are formed within 4.26 ns of each other.

Like δt, the lifetime of interface defects, τ, can also be measured. As shown in Fig. 2f, τ seems linear in the log-log histogram, which is the signature of a power-law distribution, $f_\tau \propto \tau^{-\alpha}$. This distribution is known to be heavy-tailed, meaning that the tail of the power-law distribution is not exponentially bound[39]. However, as seen in Fig. 2f, this is not the case for τ, as there are no interface defects with a lifetime longer than around 5 ns. Thus, it is suitable to model τ as a power-law distribution with an exponential cutoff whose PDF is given by

$$f_\tau = \frac{\lambda_2^{1-\alpha}}{\Gamma(1-\alpha, \lambda_2 \tau_{\min})} \tau^{-\alpha} e^{-\lambda_2 \tau}, \tag{2}$$

here $\Gamma(1 - \alpha, \lambda_2\tau_{min})$ is the upper incomplete gamma function. For details on the derivation of Eq. (2) and its CDF see Supplementary Information Section 3. Fitting the CDF of Eq. (2) to the normalized cumulative sum of the measured values of τ yields $\alpha = 1.20$, $\lambda_2 = 1.04 \cdot 10^9$ s^{-1} and $\tau_{min} = 1.10 \cdot 10^{-12}$ s. This gives an expected value for the lifetime of interface defects, $\langle\tau\rangle = \frac{1}{\lambda_2}\frac{\Gamma(2-\alpha, \lambda_2\tau_{min})}{\Gamma(1-\alpha, \lambda_2\tau_{min})} = 0.082$ ns and from the CDF, it is found that 99% of all interface defects have a lifetime shorter than 1.17 ns.

To study how δt and τ are influenced by various growth conditions such as growth rate k or temperature T, a snapshot was extracted from the growth of the (6,5) SWCNT (Sim. 1 in Extended Data Table 1) and MD simulations were performed for 1 to 2 µs at different temperatures without adding any carbon atoms to the system (Sim. 2-6 in Extended Data Table 1). These simulations represent conditions closer to experimental growth, where the growth rate is approximately 50 to 1000 times lower than what was used in Sim. 1. From Extended Data Table 1, an approximately 7% reduction in $\langle\delta t\rangle$ is observed for the faster-growing SWCNT in Sim. 1 compared to Sim. 4. Longer interface defect lifetimes are also seen for Sim. 1, with an approximately 82% larger $\langle\tau\rangle$ compared to Sim. 4. However, given that the growth rate in Sim. 1 is more than 640 times higher than in Sim. 4, it is concluded that both the time between the formation of interface defects and their lifetimes are largely independent of the growth rate. In contrast, the growth temperature significantly affects both δt and τ. By comparing the MD simulations of the extracted snapshot performed at different temperatures (Sim. 2-6 in Extended Data Table 1), it is evident that as the temperature decreases, δt increases significantly. With a 2 to 3 times increase in $\langle\delta t\rangle$ observed for only a 100 K decrease in growth temperature. Similarly, $\langle\tau\rangle$ increases with a decrease in temperature, although here the effect is less pronounced, with only a 15 to 30% increase for a 100 K decrease in temperature.

Impact of growth conditions on defect-free growth

For reliable production of long, defect-free CNTs with uniform properties over their entire length, it is crucial to understand how growth rate and temperature affect the entrapment of interface defects. Thus, a simple model is proposed for the expected length, in terms of the number of carbon atoms, $\langle N_C \rangle$, that a CNT can reach during growth before an interface defect is likely to be trapped. As detailed in Supplementary Information Section 4, this model is based on the distributions that model the interface defects, Eq. (1) and (2), and gives the expected length as

$$\langle N_C \rangle = \frac{k}{\lambda_1} \frac{\Gamma(1-\alpha, \lambda_2 \tau_{min})}{\Gamma\left(1-\alpha, \lambda_2 \frac{2}{k}\right)}. \tag{3}$$

Here, k is the growth rate of the CNT, while α, λ_1, λ_2, and τ_{min} are the parameters from Eq. (1) and (2). Though Eq. (3) accounts for the effect of the growth rate on the expected length, $\langle N_C \rangle$, the impact of growth temperature is absent. This can be addressed by including the temperature effects on δt and τ, as demonstrated in Extended Data Table 1, by modeling the temperature behavior of α, λ_1, λ_2 and τ_{min} as shown in Extended Data Fig. 3. Combined with Eq. (3) it is now possible to construct a map of the estimated defect-free CNT length for different combinations of growth rates and temperatures.

The map in shown in Fig. 3a reveals two growth regimes with a sharp transition, a light blue region representing growth conditions resulting in defective tubes and a dark blue region representing growth conditions favorable for growing long defect-free tubes. Experimentally, the growth rate of CNTs has been correlated to the partial pressure, P, of the carbon feedstock gas (supply of carbon atoms), increasing monotonically with pressure[40-42].
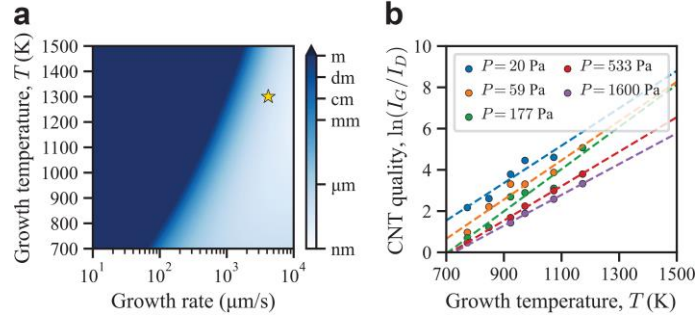
Fig. 3: Influence of growth rate and temperature on defect-free CNT growth. The 2D map in **a** show the expected length that a CNT can grow before an interface defect is trapped. Here the expected length, calculated using Eq. (3), is converted to meters through multiplication with $8.35 \cdot 10^{-12}$ m per C atoms. Corresponding to the length per carbon atom of a (11,3) SWCNT with a diameter of 1 nm and a gold star marks the growth conditions used to produce the (6,5) SWCNT in Fig. 2. The plot in **b** shows the quality of CNTs grown under different experimental conditions, T and P, as determined by the ratio of G-band, I_G, and D-band, I_D, Raman intensities. Here the markers are reproduced from the published experimental data of Picher et al.[43] and the dashed lines are a linear regression to this data.

203   From Fig. 3a it is evident that for a set growth temperature, decreasing the growth rate, i.e.,

204   lowering the partial pressure, P, results in higher quality CNTs (growth of long defect-free tubes).

205   Likewise, for a set growth rate (partial pressure), increasing the growth temperature will increase

206   the quality of the grown CNTs. These results agree remarkably well with the experimental results

207   of Picher et al.[43] presented in Fig. 3b where the same qualitative trends can be found. Independent

208   experimental results from Vinten et al.[44] also directly support this.

209   Obtaining higher quality CNTs at lower growth rates is easily understood as low growth rates

210   allow more time for defects to heal. However, higher quality CNTs at higher growth temperatures

211   might seem counterintuitive, given that high growth temperatures decrease $\langle \delta t \rangle$, leading to the

212   formation of more interface defects as shown in Extended Data Table 1. But the reduction in $\langle \tau \rangle$

213   at high temperatures decreases the likelihood of these interface defects becoming trapped inside

214   the tube wall during growth, counteracting the increased rate of formation of interface defects.

215   Consequently, if the growth rate (partial pressure) is appropriately chosen to match the growth

216   temperature there is theoretically no upper limit to the length of defect-free CNTs that can be

217   grown. Moreover, higher growth temperatures enable faster growth of long defect-free CNTs, if

218   the carbon supply rate can be controlled. Both can be achieved by carefully tuning the growth

219   conditions to control the decomposition of the precursor gas at the growth temperature while

220   maintaining stable conditions.

221   **Dynamics of the tube-catalyst interface**

222   As shown, growth including the formation and healing of interface defects occur at the tube-

223   catalyst interface. Therefore, it becomes crucial to study how the tube-catalyst interface evolves

224   during growth, which has a direct impact on the current understanding of growth mechanisms[14, 15,

225   45-47]. By tracking the configuration of the SWCNT-edge during growth, the dynamics of the tube-

226   catalyst interface can be studied. For the growth of the (6,5) SWCNT, the complete evolution of

227   the tube-catalyst interface can be observed in Extended Data Video 4, from which the 9 most

228   common edge configurations are shown in Fig. 4a. These make it evident that the tube-catalyst

229   interface is highly dynamic throughout growth, with a varying number of armchair pairs, N_A, and

230   zigzag sites, N_Z, and does not evolve in a continuous spiral growth mode[14].

231   To compare the evolution of the tube-catalyst interface, an edge chiral index (n_e, m_e) is derived,

232   where $n_e = N_A + N_Z$ and $m_e = N_A$. Identifying edges with the same number of armchair pairs and

233   zigzag sites as the "natural" perpendicular cut edge of a SWCNT with chirality (n, m) becomes

234   straightforward with this approach, as $n_e = n$ and $m_e = m$ in these instances. Fig. 4b shows the

235   distribution of the edge chiral index after the formation of the SWCNT-cap for the defect-free
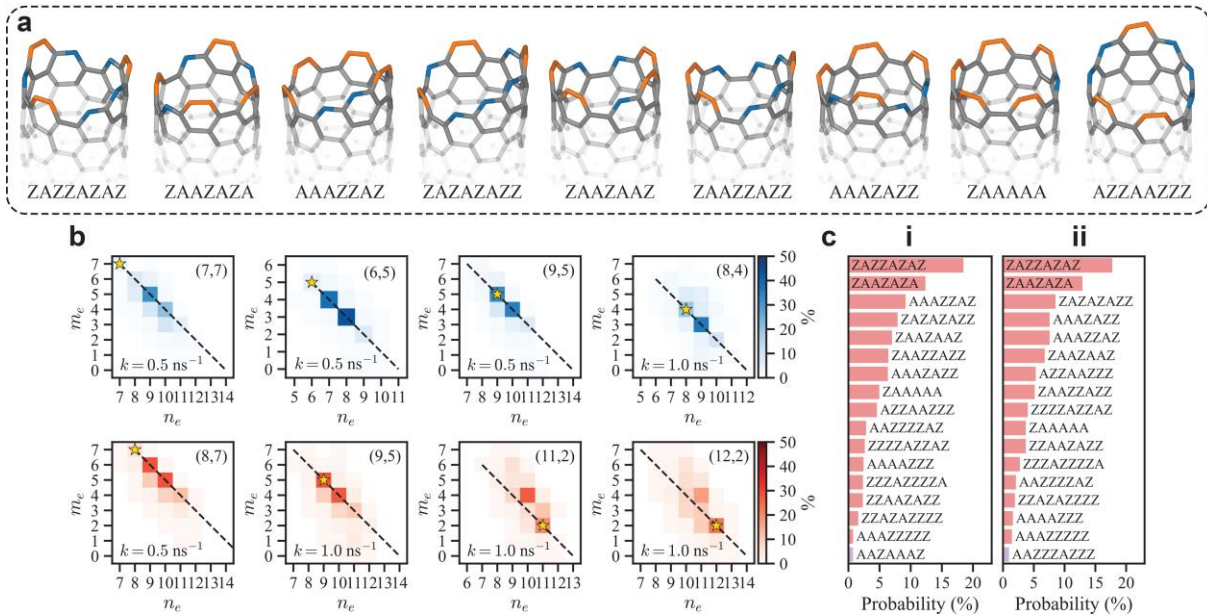
236   SWCNTs grown.

Fig. 4: Edge configurations observed during growth of SWCNTs on a Fe$_{55}$ catalyst. Panel **a** show the 9 most common interfaced observed during growth of the (6,5) SWCNT in Fig. 2. Here zigzag sites are denoted by Z and colored blue in the structure while armchair pairs are denoted by A and colored orange. **b** 2D histograms showing the distribution of edge chiral indices for different tubes grown at 1300 K (blue) and 1500 K (red). Here the chirality (n, m) of the final grown tube is shown in the upper right corner of the 2D histograms and marked by the gold star. The dashed line shows where the length of the edge, $n_e + m_e$, matches the length of the "natural" perpendicularly cut edge of the final grown tube, $n + m$. For each SWCNT its growth rate is denoted by k in the histograms. **c** bar graph of the 17 most observed edge configurations during **i** the entire growth simulation of the (6,5) SWCNT and **ii** just before the formation of an interface defect. Here the color of the bars represents the length of the edge where green: $n_e + m_e = 10$, red: 11 and purple: 12 atoms.

Intriguingly, the most dominant edge chiral index does not necessarily match the chirality of the grown tube. For the (6,5) SWCNT, the most dominant edge, with a probability of 43.3%, is $(n_e, m_e) = (8,3)$, closely followed by $(n_e, m_e) = (7,4)$ with a probability of 37.3%. These two edge chiral indices account for 80.6% of all edge chiral indices observed during growth, hinting at the importance of the configurational entropy of the SWCNT-edge[15]. This drives the edge to be

chiral, regardless of the tube chirality, as can be seen by comparing the (n_e, m_e) distributions for the (7,7) and (9,5) SWCNTs in Fig. 4b.

The edge chiral index, however, does not uniquely identify a SWCNT-edge, as there are multiple ways to arrange N_A and N_Z. Confirming the importance of configurational entropy thus requires checking whether a preferred edge configuration or set of configurations emerges during growth. This is done by counting the occurrence of each unique edge configuration, accounting for the cyclic nature of the edge. As shown in Fig. 4ci, the most frequently observed edge configuration during growth of the (6,5) SWCNT is ZAZZAZAZ with a probability of 18.5%, closely followed by ZAAZAZA (12.4%), AAAZZAZ (9.18%), and so on. Thus, there is no preferred edge configuration or set of configurations during growth, confirming the importance of configurational entropy—which has not only been shown to affect stability[15] but also indirectly evidenced via dynamic instabilities in experimentally measured growth kinetics[47, 48]. Additional data on the most frequently observed edge configurations for the other defect-free SWCNTs grown can be found in Extended Data Fig. 4. By comparing the edge configurations present just before the formation of interface defects, Fig. 4cii, to those of all the edges seen during growth, Fig. 4ci, it is apparent that formation of interface defects does not depend on the configuration of the edge but instead is purely stochastic.

The quality of the DeepCNT-22 MLFF and its ability to drive long-timescale simulations, enabled us to probe the dynamics of growing carbon nanotube interfaces. Large fluctuations in armchair and zigzag edge atoms were observed during growth. This demonstrates the importance of configurational entropy, affecting both their ordering and numbers. Formation and healing of interface defects are shown to depend on the interplay between the growth rate and temperature, paving the way for the controlled synthesis of long, defect-free CNTs. In the future, this renewed

265 understanding of the growth mechanisms should be extended to elemental or alloyed catalysts that

266 remain stiffer and less compliant under growth which may promote chiral selectivity[49].

267 **Main References:**

268 1. Iijima, S. Helical microtubules of graphitic carbon. *Nature* **354**, 56-58 (1991).

269 2. Zhang, M., Atkinson, K. R. & Baughman, R. H. Multifunctional Carbon Nanotube Yarns by Downsizing an
270 Ancient Technology. *Science* **306**, 1358-1361 (2004).

271 3. Zhong, D. *et al*. Gigahertz integrated circuits based on carbon nanotube films. *Nature electronics* **1**, 40-45 (2017).

272 4. Fang, R. *et al*. Single-wall carbon nanotube network enabled ultrahigh sulfur-content electrodes for high-
273 performance lithium-sulfur batteries. *Nano energy* **42**, 205-214 (2017).

274 5. Jiang, S. *et al*. Ultrahigh-performance transparent conductive films of carbon-welded isolated single-wall carbon
275 nanotubes. *Science Advances* **4**, eaap9264 (2018).

276 6. Dresselhaus, M. S., Dresselhaus, G. & Saito, R. Physics of carbon nanotubes. *Carbon* **33**, 883-891 (1995).

277 7. Zheng, L. X. *et al*. Ultralong single-wall carbon nanotubes. *Nat Mater* **3**, 673-676 (2004).

278 8. Wang, X. *et al*. Fabrication of Ultralong and Electrically Uniform Single-Walled Carbon Nanotubes on Clean
279 Substrates. *Nano Lett.* **9**, 3137-3141 (2009).

280 9. Zhang, R. *et al*. Growth of Half-Meter Long Carbon Nanotubes Based on Schulz–Flory Distribution. *ACS Nano* **7**,
281 6156-6161 (2013).

282 10. Charlier, J. C. Defects in Carbon Nanotubes. *Acc. Chem. Res.* **35**, 1063-1069 (2002).

283 11. Jourdain, V. & Bichara, C. Current understanding of the growth of carbon nanotubes in catalytic chemical
284 vapour deposition. *Carbon* **58**, 2-39 (2013).

285 12. Page, A. J., Ding, F., Irle, S. & Morokuma, K. Insights into carbon nanotube and graphene formation
286 mechanisms from molecular simulations: a review. *Rep. Prog. Phys.* **78**, 036501 (2015).

287 13. Unke, O. T. *et al*. Machine Learning Force Fields. *Chem. Rev.* **121**, 10142-10186 (2021).

288 14. Ding, F., Harutyunyan, A. R. & Yakobson, B. I. Dislocation theory of chirality-controlled nanotube growth.
289 *PNAS* **106**, 2506-2509 (2009).

290 15. Magnin, Y., Amara, H., Ducastelle, F., Loiseau, A. & Bichara, C. Entropy-driven stability of chiral single-
291 walled carbon nanotubes. *Science* **362**, 212-215 (2018).

292 16. Takakura, A. *et al*. Strength of carbon nanotubes depends on their chemical structures. *Nature Communications*
293 **10**, 3040-7 (2019).

294 17. Pop, E., Mann, D., Wang, Q., Goodson, K. & Dai, H. Thermal Conductance of an Individual Single-Wall
295 Carbon Nanotube above Room Temperature. *Nano letters* **6**, 96-100 (2005).

296 18. Wilder, J. W. G., Venema, L. C., Rinzler, A. G., Smalley, R. E. & Dekker, C. Electronic structure of atomically
297 resolved carbon nanotubes. *Nature* **391**, 59-62 (1998).

298 19. Bachilo, S. M. *et al*. Structure-Assigned Optical Spectra of Single-Walled Carbon Nanotubes. *Science* **298**,
299 2361-2366 (2002).

300 20. Ding, L. P. *et al*. Why Carbon Nanotubes Grow. *J. Am. Chem. Soc.* **144**, 5606-5613 (2022).

301 21. Yao, Y., Liu, R., Zhang, J., Jiao, L. & Liu, Z. Raman Spectral Measuring of the Growth Rate of Individual
302 Single-Walled Carbon Nanotubes. *The Journal of Physical Chemistry C* **111**, 8407-8409 (2007).

303 22. Unrau, C. J., Axelbaum, R. L. & Fraundorf, P. Single-walled carbon nanotube formation on iron oxide catalysts
304 in diffusion flames. *J Nanopart Res* **12**, 2125-2133 (2009).

305 23. Hofmann, S. *et al*. In situ Observations of Catalyst Dynamics during Surface-Bound Carbon Nanotube
306 Nucleation. *Nano letters* **7**, 602-608 (2007).

307 24. Yoshida, H., Takeda, S., Uchiyama, T., Kohno, H. & Homma, Y. Atomic-Scale In-situ Observation of Carbon
308 Nanotube Growth from Solid State Iron Carbide Nanoparticles. *Nano Lett.* **8**, 2082-2086 (2008).

309 25. Yang, F. *et al*. Growth modes of single-walled carbon nanotubes on catalysts. *Science advances* **8**, eabq0794
310 (2022).

311 26. Neyts, E. C., Shibuta, Y., van Duin, Adri C. T & Bogaerts, A. Catalyzed Growth of Carbon Nanotube with
312 Definable Chirality by Hybrid Molecular Dynamics−Force Biased Monte Carlo Simulations. *ACS nano* **4**, 6665-
313 6672 (2010).

314 27. Xu, Z., Yan, T. & Ding, F. Atomistic simulation of the growth of defect-free carbon nanotubes. *Chemical
315 Science* **6**, 4704-4711 (2015).

316 28. Yoshikawa, R. *et al*. Molecular Dynamics of Chirality Definable Growth of Single-Walled Carbon Nanotubes.
317 *ACS nano* **13**, 6506-6512 (2019).

318 29. Deringer, V. L. *et al*. Origins of structural and electronic transitions in disordered silicon. *Nature* **589**, 59-64
319 (2021).

320 30. Wang, H., Zhang, L., Han, J. & E, W. DeePMD-kit: A deep learning package for many-body potential energy
321 representation and molecular dynamics. *Computer Physics Communications* **228**, 178-184 (2018).

322 31. Ding, F. *et al*. The Importance of Strong Carbon−Metal Adhesion for Catalytic Nucleation of Single-Walled
323 Carbon Nanotubes. *Nano Lett.* **8**, 463-468 (2007).

324 32. Silvearv, F., Larsson, P., Jones, S. L. T., Ahuja, R. & Larsson, J. A. Establishing the most favorable metal–
325 carbon bond strength for carbon nanotube catalysts. *J. Mater. Chem. C* **3**, 3422-3427 (2015).

326 33. Ceriotti, M., Tribello, G. A. & Parrinello, M. Simplifying the representation of complex free-energy landscapes
327 using sketch-map. *Proceedings of the National Academy of Sciences* **108**, 13023-13028 (2011).

328 34. Ding, F., Bolton, K. & Rosén, A. Nucleation and Growth of Single-Walled Carbon Nanotubes: A Molecular
329 Dynamics Study. *The journal of physical chemistry. B* **108**, 17369-17377 (2004).

330 35. Ribas, M. A., Ding, F., Balbuena, P. B. & Yakobson, B. I. Nanotube nucleation versus carbon-catalyst adhesion–
331 Probed by molecular dynamics simulations. *The Journal of chemical physics* **131**, 224501 (2009).

332 36. Qiu, L. & Ding, F. Is the Carbon Nanotube-Catalyst Interface Clean during Growth? *Small* **18**, e2204437-n/a
333 (2022).

334 37. Amara, H., Bichara, C. & Ducastelle, F. Understanding the Nucleation Mechanisms of Carbon Nanotubes in
335 Catalytic Chemical Vapor Deposition. *Physical review letters* **100**, 056105 (2008).

336 38. Page, A. J., Ohta, Y., Irle, S. & Morokuma, K. Mechanisms of Single-Walled Carbon Nanotube Nucleation,
337 Growth, and Healing Determined Using QM/MD Methods. *Acc. Chem. Res.* **43**, 1375-1385 (2010).

338 39. Asmussen, S. R. in *Steady-State Properties of GI/G/1* 266–301 (Wiley & Sons, 2008).

339 40. Einarsson, E., Murakami, Y., Kadowaki, M. & Maruyama, S. Growth dynamics of vertically aligned single-
340 walled carbon nanotubes from in situ measurements. *Carbon* **46**, 923-930 (2008).

341 41. Picher, M., Anglaret, E., Arenal, R. & Jourdain, V. Self-Deactivation of Single-Walled Carbon Nanotube
342 Growth Studied by in Situ Raman Measurements. *Nano letters* **9**, 542-547 (2009).

343 42. In, J. B., Grigoropoulos, C. P., Chernov, A. A. & Noy, A. Growth Kinetics of Vertically Aligned Carbon
344 Nanotube Arrays in Clean Oxygen-free Conditions. *ACS nano* **5**, 9602-9610 (2011).

345 43. Picher, M. *et al*. Influence of the growth conditions on the defect density of single-walled carbon nanotubes.
346 *Carbon* **50**, 2407-2416 (2012).

347 44. Vinten, P., Marshall, P., Lefebvre, J. & Finnie, P. Thermodynamic and Energetic Effects on the Diameter and
348 Defect Density in Single-Walled Carbon Nanotube Synthesis. *The Journal of Physical Chemistry C* **117**, 3527-3536
349 (2013).

350 45. Liu, Y., Dobrinsky, A. & Yakobson, B. I. Graphene Edge from Armchair to Zigzag: The Origins of Nanotube
351 Chirality? *Phys. Rev. Lett.* **105**, 235502 (2010).

352 46. Hedman, D. & Larsson, J. A. Analytical modelling of single-walled carbon nanotube energies: the impact of
353 curvature, length and temperature. *SN Applied Sciences* **2** (2020).

354 47. Förster, G. D. *et al*. Swinging Crystal Edge of Growing Carbon Nanotubes. *ACS Nano* **17**, 7135-7144 (2023).

355 48. Pimonov, V. *et al*. Dynamic Instability of Individual Carbon Nanotube Growth Revealed by In Situ Homodyne
356 Polarization Microscopy. *Nano letters* **21**, 8495-8502 (2021).

357 49. Yang, F. *et al*. Chirality-specific growth of single-walled carbon nanotubes on solid alloy catalysts. *Nature* **510**,
358 522-524 (2014).

Methods:

To create the DeepCNT-22 dataset, an initial set of structures was generated using various

methods, including molecular dynamics (MD) driven by density functional tight binding,

randomly perturbed structures, and carbon allotropes from the GAP-20 dataset[1]. After which the

dataset was further refined using a variant of the active learning scheme[2-4], in which an ensemble

of machine learning force fields (MLFFs) is trained on the dataset and employed to drive MD

simulations of single-walled carbon nanotube (SWCNT) growth. During this process, the deviation in the MLFFs' force predictions (i.e., model deviation) is utilized to identify unrepresented structures that emerge during the growth process, which are then labeled and added to the dataset such that a new ensemble of MLFFs can be trained. This procedure is repeated until the model deviation remains low throughout the growth simulation. Regardless of the generation method, all structures were labeled with energies and forces obtained via dispersion-corrected density functional theory (DFT) calculations.

After training, the DeepCNT-22 MLFF was used to drive MD simulations of SWCNT growth. Extended Data Video 1, 2, 3 and 4 were then generated from the MD trajectory of the grown (6,5) SWCNT. Post-growth, the SWCNT structure was adjusted to align its axis parallel to the z-axis. Videos were subsequently rendered from the aligned MD trajectory using the OVITO software package[5]. The Smooth trajectory modifier, available in OVITO, with a window size of 5 was applied to minimize thermal vibrations and highlight the evolution of the structure during growth. Visualization of the tube-catalyst interface as shown in Extended Data Video 4, involved removing all iron atoms and then iteratively removing carbon atoms with a coordination number less than 2 until only those with a coordination number of 2 or higher remained.

Density functional tight binding

The initial dataset for DeepCNT-22 includes structures obtained from density functional tight binding (DFTB) MD simulations of SWCNT nucleation originating from atomic carbon precursors on Fe nanoparticle catalysts. DFTB is an extended two-center Hückel approximation to DFT, employing a minimal Slater-type all valence basis set. This allows dynamic simulations to occur orders of magnitude faster than DFT, while including electronic effects not found in classical force field-based methods. MD simulations relied on self-consistent charge DFTB (SCC-DFTB)[6] to

19

388   compute quantum chemical potential energy and energy gradients during each MD iteration. The

389   trans3d-0-1 parameter set was used[7], with all simulations conducted within the DFTB+ software

390   package[8] version 21.1. Newton's equations of motion were integrated using the velocity-Verlet

391   algorithm[9], with a 1.0 fs time step and a finite electronic temperature of 10,000 K[10-12]. A canonical

392   NVT ensemble was maintained at 1500 K using a Nosé-Hoover chain thermostat[13-15] of length 3.

393   Structures were procured from MD simulations include Fe_{13}, Fe_{38}, or Fe_{55} nanoparticles within a

394   periodic cell without C atoms, or with 20, 30, or 40 C atoms for the case of Fe_{13}. Extracted

395   structures from these simulations featured Fe nanoparticles with surface-adsorbed carbon

396   monomers and dimers, carbon chains and junctions, ring networks frequently containing defects,

397   and SWCNT-cap and tube-like structures, consistent with previous DFTB growth simulations[16,

398   17]. DFTB MD simulations were also used to anneal high-energy structures obtained by early

399   versions of the MLFF, with the resulting structures added to the dataset. To identify which

400   structures from the DFTB MD simulations to label with DFT and include in the training data,

401   farthest point sampling was conducted on the DFTB calculated potential energies.

402   **Density function theory**

403   DFT calculations were performed using the Vienna Ab initio Simulation Package (VASP)[18-20]

404   version 6.3.0. A plane wave basis set was employed, and the projector-augmented wave method[21,

405   22] was utilized with standard pseudopotentials (Fe 06Sep2000 and C 08Apr2002). The optB86b-

406   vdW van der Waals density functional[23, 24] was selected to account for dispersion interactions.

407   High precision (PREC = Accurate) was employed throughout the calculations, with a plane wave

408   cutoff energy of 600 eV (ENCUT = 600) and no symmetry constraints applied (ISYM = 0). To

409   ensure accuracy, the electronic self-consistent loop converged to a tolerance of 10^{-6} eV (EDIFF =

410   1.0E-6). Gaussian smearing (ISMEAR = 0) was utilized with a smearing width of 0.05 eV (SIGMA

411 = 0.05) to assist in the convergence of the calculations. Spin-polarized calculations were conducted

412 (ISPIN = 2), with a high initial magnetic moment, 3 μ_B, assigned to each Fe atom. For all periodic

413 structures, a Γ-centered k-point mesh with a density of 0.25 Å^{-1} (KSPACING = 0.25) was used,

414 while for non-periodic structures, only the Γ-point was used with a minimum of 10 Å vacuum

415 spacing between periodic images. Only single point calculations were performed, as DFT

416 calculations were utilized to label the training data.

417 **Machine learning force field**

418 DeepCNT-22 is built on the Deep Potential-Smooth Edition architecture[25] and was developed

419 using DeePMD-kit[26] version 2.1.1. This MLFF is of the Behler-Parrinello type[27], wherein the

420 energy of each atom in a structure is predicted using a neural network, and subsequently summed

421 to yield the total energy of the structure. A type map of [Fe, C] was utilized together with the type

422 embedding approach, which improves performance and accuracy by allowing the use of a single

423 descriptor embedding net and fitting net shared by both atom types. For further information on the

424 Deep Potential-Smooth Edition architecture and the type embedding approach, consult the

425 DeePMD-kit documentation[28].

426 Utilizing the type embedding approach, an embedding net with 2 hidden layers containing 8

427 neurons each was employed. The descriptor embedding net was of type se_e2_a and consisted of

428 3 hidden layers with 16, 32, and 64 neurons, as well as 8 axis neurons. A cutoff of 5.0 Å was

429 applied to define each atom's local environment, with a smooth cutoff of 0.5 Å, and a fitting net

430 comprising 3 hidden layers with 256 neurons each was used. The GELU activation function[29] was

431 applied for each hidden layer, and no timestep was used in the ResNet architecture[30]. During

432 training, the following loss function was applied, $\mathcal{L} = \frac{p_\epsilon}{N} \Delta E^2 + \frac{p_f}{3N} |\Delta \boldsymbol{F}|^2$, where N denotes the

433 number of atoms, E the energy, and $\boldsymbol{F}$ the forces acting on each structure. Energy and force error

weights, p_ϵ and p_f, were set to 0.1 and 1.0, respectively, and remained constant during training. Training was performed for 300,000 batches, using a batch size of 5 structures and the Adam optimizer[31] with an initial learning rate of 10^{-3}, which decayed exponentially to 10^{-5} by the end of the training.

Molecular dynamics

MD simulations of SWCNT growth were performed using the Large-scale Atomic/Molecular Massively Parallel Simulator (LAMMPS)[32] version 29 Sep 2021 - Update 3, with the deepmd pair style and the DeepCNT-22 MLFF. The nsq algorithm was employed for neighbor list construction with a cutoff distance of 5.0 Å, as it offers slight performance advantages for smaller systems. A 2.0 Å skin distance was incorporated, and the neighbor list was only rebuilt if at least one atom moved more than half the skin distance. Simulations took place in the NVT ensemble using a Nosé-Hoover chain thermostat[13-15] of length 3, and a temperature damping parameter of 0.1 ps. The equations of motion were integrated with a 2.0 fs timestep, maximizing performance while maintaining simulation stability. Initial atom velocities were drawn from a Gaussian distribution, and the resulting ensemble of velocities had linear and angular momenta zeroed before being scaled to correspond to the growth temperature T. Fe and C atom masses were set to 55.847 u and 12.011 u, respectively. C atoms were introduced individually at a rate of k ns^{-1} within a spherical deposit region of radius $d_C/4$ located at the center of the simulation box, here d_C is diameter of the Fe catalyst. To guarantee carbon atoms were consistently deposited inside the Fe catalyst, the system was recentered after every timestep, ensuring that the catalyst remained at the center of the simulation box. The number of degrees of freedom contributing to the system temperature was dynamically updated to account for the newly deposited carbon atoms. Simulation data, including system temperature, potential energy, number of 0, 1, 2, and 3 carbon-carbon coordinated atoms,

total number of carbon atoms added, and atomic coordinates, energies, and carbon-carbon

coordination numbers, was recorded to disk every 2 ps for subsequent analysis.

Data availability:

Both the DeepCNT-22 MLFF and the dataset used to train it as well as the entire MD trajectory

from the growth simulation of the (6,5) single-walled carbon nanotube will be available online

(Zenodo) upon journal publication.

Code availability:

All code required to run MD simulations of SWCNT growth using the DeepCNT-22 MLFF

together with LAMMPS will be available online (Zenodo) upon journal publication.

Methods references:

1. Rowe, P., Deringer, V. L., Gasparotto, P., Csányi, G. & Michaelides, A. An accurate and transferable machine learning potential for carbon. *J. Chem. Phys.* **153**, 034702 (2020).

2. Podryabinkin, E. V. & Shapeev, A. V. Active learning of linearly parametrized interatomic potentials. *Computational materials science* **140**, 171-180 (2017).

3. Smith, J. S., Nebgen, B., Lubbers, N., Isayev, O. & Roitberg, A. E. Less is more: Sampling chemical space with active learning. *J. Chem. Phys.* **148**, 241733 (2018).

4. Zhang, L., Lin, D., Wang, H., Car, R. & E, W. Active learning of uniformly accurate interatomic potentials for materials simulation. *Phys. Rev. Mater.* **3**, 023804 (2019).

5. Stukowski, A. Visualization and analysis of atomistic simulation data with OVITO–the Open Visualization Tool. *Modelling Simul. Mater. Sci. Eng.* **18**, 015012 (2009).

6. Elstner, M. *et al*. Self-consistent-charge density-functional tight-binding method for simulations of complex materials properties. *Phys. Rev. B* **58**, 7260-7268 (1998).

7. Zheng, G. *et al*. Parameter Calibration of Transition-Metal Elements for the Spin-Polarized Self-Consistent-Charge Density-Functional Tight-Binding (DFTB) Method: Sc, Ti, Fe, Co, and Ni. *J. Chem. Theory Comput.* **3**, 1349-1367 (2007).

8. Hourahine, B. *et al*. DFTB+, a software package for efficient approximate density functional theory based atomistic simulations. *The Journal of chemical physics* **152**, 124101 (2020).

484   9. Swope, W. C., Andersen, H. C., Berens, P. H. & Wilson, K. R. A computer simulation method for the calculation
485   of equilibrium constants for the formation of physical clusters of molecules: Application to small water clusters. *The*
486   *Journal of chemical physics* **76**, 637-649 (1982).

487   10. Weinert, M. & Davenport, J. W. Fractional occupations and density-functional energies and forces. *Phys. Rev. B*
488   **45**, 13709-13712 (1992).

489   11. Wentzcovitch, R. M., Martins, J. L. & Allen, P. B. Energy versus free-energy conservation in first-principles
490   molecular dynamics. *Phys. Rev. B* **45**, 11372-11374 (1992).

491   12. Wagner, F., Laloyaux, T. & Scheffler, M. Errors in Hellmann-Feynman forces due to occupation-number
492   broadening and how they can be corrected. *Phys. Rev. B* **57**, 2102-2107 (1998).

493   13. Nosé, S. A unified formulation of the constant temperature molecular dynamics methods. *The Journal of*
494   *chemical physics* **81**, 511-519 (1984).

495   14. Hoover, W. G. Canonical dynamics: Equilibrium phase-space distributions. *Phys. Rev. A* **31**, 1695-1697 (1985).

496   15. Martyna, G. J., Klein, M. L. & Tuckerman, M. Nosé–Hoover chains: The canonical ensemble via continuous
497   dynamics. *The Journal of Chemical Physics* **97**, 2635-2643 (1992).

498   16. Ohta, Y., Okamoto, Y., Page, A. J., Irle, S. & Morokuma, K. Quantum Chemical Molecular Dynamics
499   Simulation of Single-Walled Carbon Nanotube Cap Nucleation on an Iron Particle. *ACS Nano* **3**, 3413-3420 (2009).

500   17. McLean, B., Mitchell, I. & Ding, F. Mechanism of alcohol chemical vapor deposition growth of carbon
501   nanotubes: Catalyst oxidation. *Carbon* **191**, 1-9 (2022).

502   18. Kresse, G. & Hafner, J. Ab initio molecular dynamics for liquid metals. *Phys. Rev. B* **47**, 558-561 (1993).

503   19. Kresse, G. & Furthmüller, J. Efficiency of ab-initio total energy calculations for metals and semiconductors
504   using a plane-wave basis set. *Computational Materials Science* **6**, 15-50 (1996).

505   20. Kresse, G. & Furthmüller, J. Efficient iterative schemes for ab initio total-energy calculations using a plane-
506   wave basis set. *Phys. Rev. B* **54**, 11169-11186 (1996).

507   21. Blöchl, P. E. Projector augmented-wave method. *Phys. Rev. B* **50**, 17953-17979 (1994).

508   22. Kresse, G. & Joubert, D. From ultrasoft pseudopotentials to the projector augmented-wave method. *Phys. Rev. B*
509   **59**, 1758-1775 (1999).

510   23. Dion, M., Rydberg, H., Schröder, E., Langreth, D. C. & Lundqvist, B. I. Van der Waals Density Functional for
511   General Geometries. *Phys. Rev. Lett.* **92**, 246401 (2004).

512   24. Klimeš, J., Bowler, D. R. & Michaelides, A. Van der Waals density functionals applied to solids. *Phys. Rev. B*
513   **83**, 195131 (2011).

514   25. Zhang, L. *et al*. End-to-end Symmetry Preserving Inter-atomic Potential Energy Model for Finite and Extended
515   Systems. *arXiv* (2018).

516 26. Wang, H., Zhang, L., Han, J. & E, W. DeePMD-kit: A deep learning package for many-body potential energy
517 representation and molecular dynamics. *Computer Physics Communications* **228**, 178-184 (2018).

518 27. Behler, J. & Parrinello, M. Generalized Neural-Network Representation of High-Dimensional Potential-Energy
519 Surfaces. *Phys. Rev. Lett.* **98**, 146401 (2007).

520 28. https://docs.deepmodeling.com/projects/deepmd.

521 29. Hendrycks, D. & Gimpel, K. Gaussian Error Linear Units (GELUs). *arXiv* (2016).

522 30. He, K., Zhang, X., Ren, S. & Sun, J. Deep Residual Learning for Image Recognition. *arXiv* (2015).

523 31. Kingma, D. P. & Ba, J. Adam: a method for stochastic optimization. *arXiv* (2014).

524 32. Thompson, A. P. *et al*. LAMMPS - a flexible simulation tool for particle-based materials modeling at the atomic,
525 meso, and continuum scales. *Computer Physics Communications* **271**, 108171 (2021).

539 **Author contributions:**

540 Investigation: DH, BM; Methodology: DH; Software: DH; Data curation: DH, BM; Formal

541 analysis: DH; Validation: DH; Conceptualization: DH, BM, CB, SM, JAL and FD; Project

542 administration: DH, FD; Funding acquisition: FD; Resources: FD, JAL; Supervision: FD;

543 Visualization: DH; Writing - original draft: DH, BM; Writing - review & editing: DH, BM, CB,
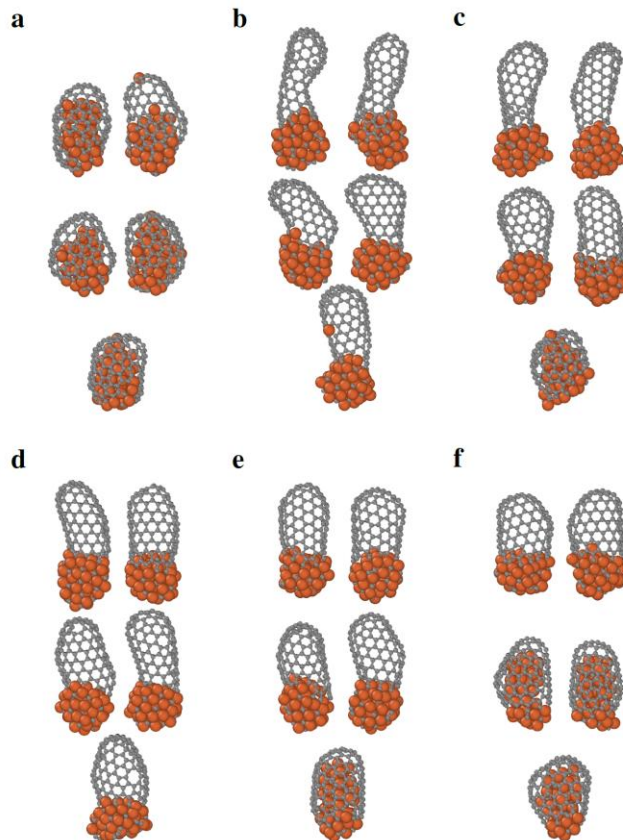
544 SM, JAL and FD

545 **Competing interests:**

546 The authors declare no competing interests.

547 **Additional information:**

548 Correspondence including requests for data/code should be addressed to Daniel Hedman

549 (daniel.hedman@ltu.se) or Feng Ding (f.ding@siat.ac.cn).

550

Extended Data Fig. 1: Effect of temperature on the growth of SWCNTs. Here tubes are grown on a Fe_{55} catalyst at a carbon supply rate of $k = 1.0$ ns^{-1}. 5 simulations were performed for each growth temperature, T, **a** 1000 K, **b** 1100 K, **c** 1200 K, **d** 1300 K, **e** 1400 K and **f** 1500K.
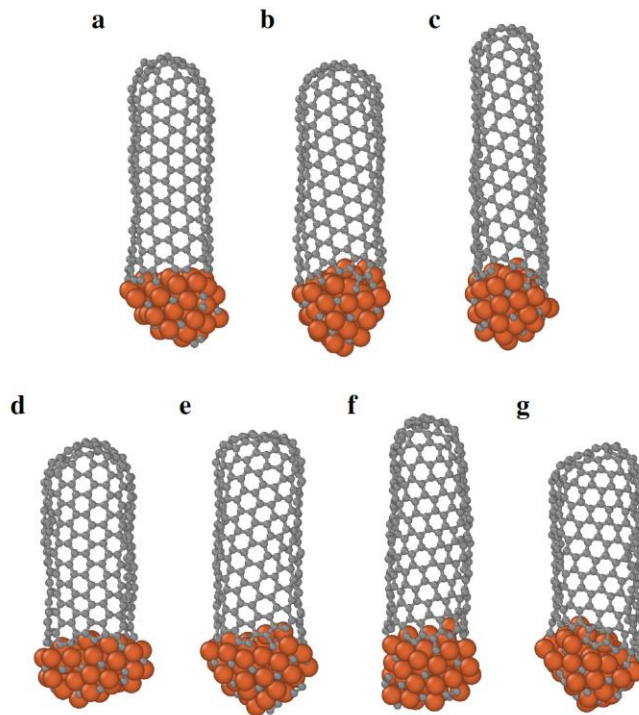
Extended Data Fig. 2: Additional long defect-free SWCNTs grown on a Fe$_{55}$ catalyst. Here **a** is a (7,7) SWCNT grown over 598 ns at T = 1300 K and a rate of k = 0.5 ns^{-1}. **b** (9,5) SWCNT grown over 598 ns at T = 1300 K and a rate of k = 0.5 ns^{-1}. **c** (8,4) SWCNT grown over 303 ns at T = 1300 K and a rate of k = 1.0 ns^{-1}. **d** (8,7) SWCNT grown over 598 ns at T = 1500 K and a rate of k = 0.5 ns^{-1}. **e** (9,5) SWCNT grown over 303 ns at T = 1500 K and a rate of k = 1.0 ns^{-1}. **f** (11,2) SWCNT grown over 303 ns at T = 1500 K and a rate of k = 1.0 ns^{-1}. **g** (12,2) SWCNT grown over 303 ns at T = 1500 K and a rate of k = 1.0 ns^{-1}.
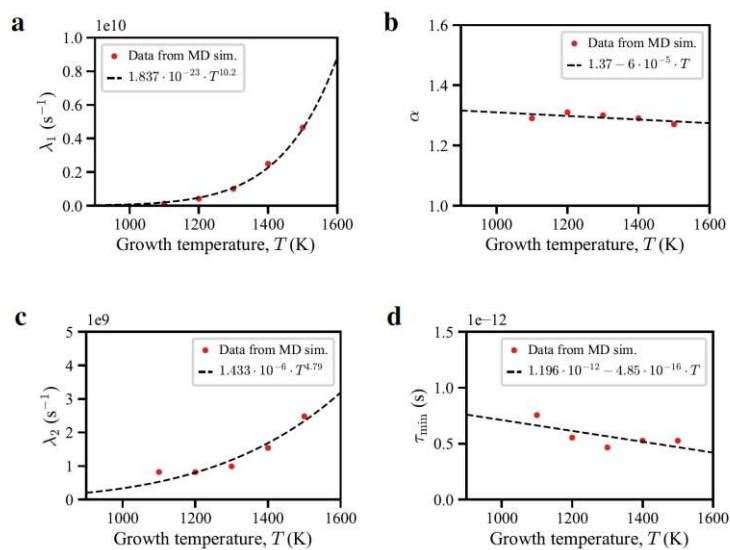
Extended Data Fig. 3: The temperature dependence of the parameters for $f_{\delta t}$ and f_τ. Here the parameter of $f_{\delta t}$ are shown in **a** and those of f_τ are shown in **b**, **c**, and **d**.

560
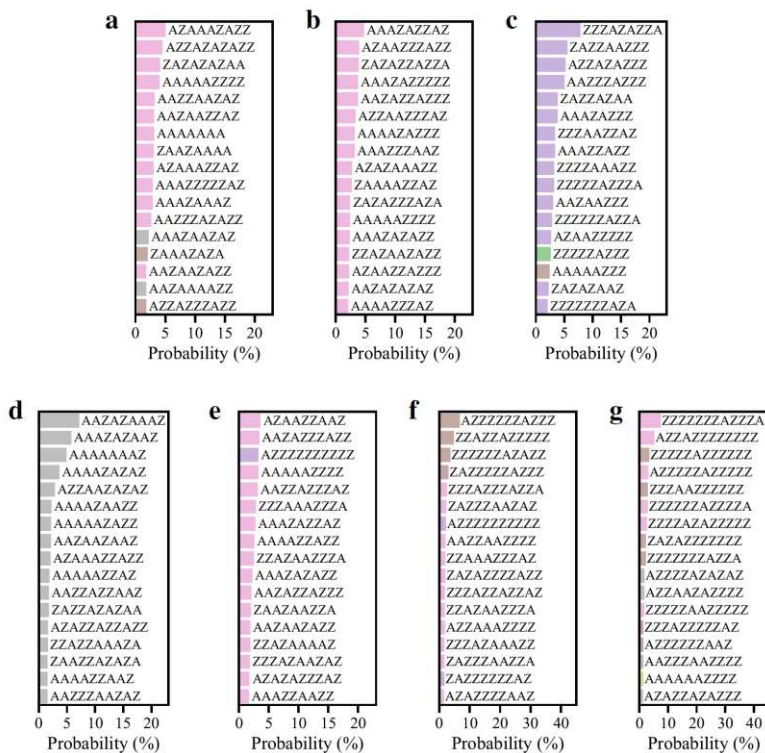
Extended Data Fig. 4: Edge configurations observed during SWCNT grown on a Fe₅₅ catalyst. The 17 most observed edge configurations during the growth of the **a** (7,7), **b** (9,5), **c** (8,4), **d** (8,7), **e** (9,5), **f** (11,2) and **g** (12,2) SWCNTs shown in Extended Data Fig. 3. Here the color of the bars represents the length of the edge where green: $n_e + m_e = 10$, red: 11, purple: 12, brown: 13, pink: 14, grey: 15 and yellow: 16 atoms.

561

562

Extended Data Table 1: Interface defect statistics. Data obtained from growth of (6,5) SWCNTs on a Fe_{55} catalyst at different conditions. Here Sim. represents the different simulations, T the growth temperature, k the carbon supply rate and t_{end} the growth time. # penta., # hepta. are the number of penta- and heptagons formed during growth, respectively. $\langle \delta t \rangle$ and $\langle \tau \rangle$ are the expectation values for the time between interface defect formation and interface defect lifetime, respectively. Note that, Sim. 1 corresponds to the growth of (6,5) SWCNTs shown in Fig. 1 while Sim. 2-6 correspond to the simulations with a constant number of carbon atoms as described in the main text.

Sim.	Growth conditions			Interface defect statistics			
	T (K)	k (ns^{-1})	t_{end} (ns)	# penta.	# hepta.	$\langle \delta t \rangle$ (ns)	$\langle \tau \rangle$ (ns)
1	1300	0.5	852	778	26	0.925	0.082
2	1500	$< 10^{-3}$	1000	4648	273	0.215	0.028
3	1400	$< 10^{-3}$	1000	2485	89	0.402	0.036
4	1300	$< 8 \cdot 10^{-4}$	1283	1287	41	0.996	0.045
5	1200	$< 10^{-3}$	1000	413	3	2.415	0.053
6	1100	$< 5 \cdot 10^{-4}$	2000	237	4	8.382	0.061

566   **Extended Data Video 1: Atomic-level details of the growth of the (6,5) SWCNT.** Atomic-level visualization of the

567   complete trajectory from the growth of the (6,5) SWCNT. Here each second of video corresponds to 3.84 ns of growth.

568

569   **Extended Data Video 2: Atomic-level details of the healing of a pentagon defect at the interface.** Atomic-level

570   visualization of the healing of a pentagon defect at the interface during the growth of the (6,5) SWCNT. Here each

571   second of video corresponds to 60 ps of simulation.

572

573   **Extended Data Video 3: Atomic-level details of the healing of a penta-heptagon defect at the interface.** Atomic-

574   level visualization of the healing of a penta-heptagon defect at the interface during the growth of the (6,5) SWCNT.

575   Here each second of video corresponds to 60 ps of simulation.

576

577   **Extended Data Video 4: Evolution of the nanotube edge during growth.** Visualization of the dynamics of the

578   nanotube edge during the growth of (6,5) SWCNTs where blue corresponds to zigzag sites, orange armchair pairs and

579   orange-green-orange are directly nucleated hexagons. Here each second of video corresponds to 3.84 ns of growth.

580

Supplementary Files

This is a list of supplementary files associated with this preprint. Click to download.

- SupplementaryInformationDeepCNT22.pdf
- extendeddatavideo1.mp4
- extendeddatavideo2.mp4
- extendeddatavideo3.mp4
- extendeddatavideo4.mp4